Relaxor ferroelectricity in the polar M2P-TCNQ charge-transfer crystal at the neutral-ionic interface

J. K H Fischer, Gabriele d'Avino, M. Masino, F. Mezzadri, P. Lunkenheimer, Z. G Soos, A. Girlando

Relaxor ferroelectricity in the polar M_2P-TCNQ charge-transfer crystal at the neutral-ionic interface

J. K. H. Fischer,[1,2,*] G. D'Avino,[3] M. Masino,[4] F. Mezzadri,[5] P. Lunkenheimer,[2] Z. G. Soos,[6] and A. Girlando[4]

[1]*Department of Advanced Materials Science, University of Tokyo, 5-1-5 Kashiwanoha, Kashiwa, Chiba 277-8561, Japan*

[2]*Experimental Physics V, Center for Electronic Correlations and Magnetism, University of Augsburg, 86159 Augsburg, Germany*

[3]*Grenoble Alpes University, CNRS, Grenoble INP, Institut Néel, 25 rue des Martyrs, 38042 Grenoble, France*

[4]*Dipartimento di Scienze Chimiche, della Vita e della Sostenibilità Ambientale (S.C.V.S.A.) & INSTM-UdR Parma, Università di Parma, 43124 Parma, Italy*

[5]*Dipartimento di Scienze Chimiche, della Vita e della Sostenibilità Ambientale (S.C.V.S.A.) & IMEM-CNR, 43124 Parma, Italy*

[6]*Department of Chemistry, Princeton University, Princeton, New Jersey 08544, USA*

(Received 3 September 2020; revised 10 December 2020; accepted 3 February 2021; published 3 March 2021)

We investigated the mixed-stack charge-transfer crystal, N,N'-dimethylphenazine-TCNQ (M_2P-TCNQ), which is polar at room temperature and just at the neutral-to-ionic interface (ionicity $\rho \approx 0.5$). We detect the typical dielectric signature of a relaxor ferroelectric and an asymmetric positive-up-negative-down behavior. While relaxor ferroelectricity is usually ascribed to disorder in the crystal, we find no evidence for structural disorder in the investigated crystals. To elucidate the origin of M_2P-TCNQ's dielectric properties we perform parallel structural and spectroscopic measurements, associated with theoretical modeling and quantum-mechanical calculations. Our combined effort points to a highly polarizable electronic system that is strongly coupled to lattice vibrations. The found indications for polarization reversal imply flipping of the bent conformation of the M_2P molecule with an associated energy barrier of a few tens of an eV, broadly consistent with an Arrhenius fit of the dielectric relaxation times. While the polarization is mostly of electronic origin, its possible reversal implies slow collective motions that are affected by solid-state intermolecular interactions.

DOI: 10.1103/PhysRevB.103.115104

I. INTRODUCTION

While spontaneous electrical polarization and ferroelectricity (FE) are well known in organic crystals [1], the focus in recent years has switched to the so-called "electronic" FE occurring in charge-transfer (CT) crystals [2–7]. The first examples of electronic FE in organic CT crystals came from the family of tetramethyltetrathiafulvalene (TMTTF) 2:1 salts [8–13]. Their FE behavior was initially unexplained, but later suggested to originate from a displacement of the anion chain accompanied by a shift of the electron holes on the donors [14]. On the other hand, the most convincing proof of electronic FE, a *P-E* hysteresis that is accompanied by the determination of *P* orientation with respect to the ion displacement, has so far only been obtained in the ionic phase of tetrathiafulvalene-chloranil (TTF-CA) [15,16], a well-known mixed-stack (ms) CT crystal undergoing the neutral-to-ionic (NI) phase transition at 80 K [17–20]. In that system, electronic FE manifested in colossal Born effective charges, whose sign is opposite that of the valence charge of molecular ions [15]. Electronic FE involves the displacement of the molecular π-electronic clouds, thus implying large values of polarization and fast response to electric fields [21]. Electronic FE is rare in ms-CT crystals at any temperature, and there is no well documented system at room temperature (RT) [22,23]. The conditions for electronic FE, i.e., polar crystals close to the NI interface, are indeed difficult to attain. In the quest for RT electronic FE, we decided to re-investigate an old ms-CT crystal [24–26], N,N'-dimethylphenazine-TCNQ (M_2P-TCNQ), polar at RT and just at the NI interface (ionicity $\rho \approx 0.5$) [27]. While the measurement of a ferroelectric *P-E* hysteresis was not achieved, we detected the typical dielectric signature of a relaxor ferroelectric, already above RT. Relaxor ferroelectrics are piezoelectric materials characterized by a peak in the T-dependent dielectric constant with a pronounced dependence on the frequency of the applied electric field. So far, a precise modeling of relaxor FE is missing [28,29]. The origin of the phenomenon is usually ascribed to the formation of clusterlike, short-range ferroelectric order (polar nanodomains). This may be caused by some form of disorder in the crystal, sometimes artificially introduced [30], but there are also examples of nominally well-ordered materials exhibiting relaxor FE, including several CT salts [31–34]. In addition to the somewhat unexpected M_2P-TCNQ relaxor properties, we also observe an unusual asymmetric positive-up-negative-down (PUND) behavior, suggestive of polarization switching.

We investigate the origin of the intriguing dielectric properties of M_2P-TCNQ by associating its structural and spectroscopic characterization to the dielectric measurements. First principle calculations and a simple semimpirical model are used to analyze the molecular and collective crystal properties, including electrical polarization, whose origin turns out

*Corresponding author: jfischer@k.u-tokyo.ac.jp

to be mostly electronic. A plausible scenario is offered to explain the relaxor behavior and the observed unique PUND features.

II. METHODS

A. X-ray diffraction

Single crystal diffraction data were collected by using a Bruker D8 Venture diffractometer equipped with a Photon CCD area detector. CuK_α radiation was used in order to gather reliable information on the absolute structure of the crystal. Low temperature was stabilized by using an Oxford Cryosystems cryostream. Data reduction was carried out by using the SADABS program [35]. SIR2019 was used for structure solution [36], and refinement was carried out full matrix by using the Shelxl program [37]. The crystal structure was refined making use of anisotropic thermal parameters for all the atoms except hydrogen, located in the difference Fourier map then constrained during the refinement.

B. Dielectric measurements

The dielectric constant and conductivity were determined using a frequency-response analyzer (Novocontrol Alpha-A). For the polarization and PUND measurements a ferroelectric analyzer (aixACCT TF2000) was used. Gold wires were attached to contacts of graphite or gold paint on opposite tips of the needlelike crystals, ensuring an electric-field direction exactly parallel to the long crystal axis (c). Sample cooling and heating was achieved by a ^{4}He-bath cryostat (Cryovac) and a nitrogen-gas cryosystem (Novocontrol Quatro).

C. Optical spectroscopy

Infrared (IR) spectra of the crystals were recorded with a Bruker IFS-66 Fourier transform spectrometer coupled to an IR microscope Hyperion 1000. Spectral resolution: 2 cm^{-1}. We used a wire-grid polarizer and a Polaroid to polarize the light in the mid-IR and near-IR regions, respectively, and a gold mirror as reference in the reflectance measurements. Due to surface irregularities of the samples, the reflectance values cannot be considered as absolute. The Raman spectra were recorded with a Renishaw 1000 Raman spectrometer equipped with the appropriate edge filter and coupled to a Leica M microscope. Various lines from a Lexel Kr laser were used for excitation. Incident and scattered polarization was controlled by a half-wave plate and a thin-film linear polarizer, respectively. A small liquid nitrogen cryostat (Linkam HFS 91) was used for temperature-dependent measurements under the IR and Raman microscopes.

D. First principles calculations

Periodic and molecular (quantum chemistry) all-electron density functional theory (DFT) calculations employed the global hybrid PBE0 functional in conjunction with the 6-31G* Gaussian basis set, unless specified otherwise. This choice ensures comparable results between the two approaches. Periodic DFT calculations were performed with the CRYSTAL17 package [38]. Quantum chemistry and hybrid quantum/classical (QM/MM) calculations were run with the ORCA code [39]. Periodic DFT calculations were performed for the *Cm* crystal structure determined in this study at 130 K. Crystal cell parameters were kept fixed to experimental values. A 2×2×2 sampling of the Brillouin zone was found sufficient to converge the properties of interest.

Brillouin-zone center (Γ point) lattice dynamics calculations were performed within the harmonic approximations according to established procedures based on the numerical evaluation of the Hessian matrix [40]. Empirical Grimme's D3 pairwise van der Waals corrections [41] were employed in phonon calculations and in the preliminary geometry optimization. Analytical Raman intensities were computed with a coupled-perturbed Kohn-Sham scheme [42,43]. Raman spectra are shown as sums of Lorentzian peaks (half-width at half-maximum of 1.5 cm^{-1}), whose amplitude is given by the squared derivative of the polarizability with respect to the normal mode coordinate.

Lattice dynamics calculations in soft molecular crystals are extremely sensitive to computational and numerical parameters. Tight tolerance criteria have hence been used for the convergence of the self-consistent field process (10^{-12} Ha for total energy) and for the optimization of atomic coordinates (1.2×10^{-4} bohr and 3×10^{-5} Ha/bohr for atomic coordinates and gradients, respectively). Very high numerical accuracy was requested for the integration grid (XXL grid) and for the truncation of bielectronic integrals (TOLINTEG 8 8 8 8 16).

A series of lattice dynamics calculations employing the PBE functional were performed to explicitly check whether using a finer sampling of the Brillouin zone (4×4×4), or upgrading the basis set by adding polarization function on hydrogens (6-31G**), or by employing triple-zeta functions (6-311G*), leads to modest variations in the vibrational frequencies. Specifically, in the most relevant frequency region below 200 cm^{-1}, these parameters determine variations in vibrational frequencies within 5 cm^{-1}. A similar matching on vibrational frequencies was found between the PBE and PBE0 functional.

The spontaneous electric polarization was calculated within the Berry phase approach [44]. To that end, we built a reference centrosymmetric structure ($C2/m$ space group) and evaluated the variation of the polarization along the path connecting the centrosymmetric and the experimental structure. We checked that no discontinuity of multiples of the polarization quantum occurs along this path [45]. The Berry phase was evaluated for Kohn-Sham eigenstates, calculated on a 8×8×8 mesh of the Brillouin zone, ensuring converged results.

Dimerization reversal (flipping) calculations consist of relaxed energy scans, i.e., geometry optimizations where the dihedral angles passing through the central N atoms of M_2P were constrained to the desired value. Molecular and solid state relaxed scans were performed with the ORCA and CRYSTAL code, respectively. The flipping of a single M_2P molecule in the M_2P-TCNQ crystal employed hybrid quantum/classical (QM/MM) calculations. The central QM subsystem (one M_2P and two neighboring TCNQ along the stack) was described at DFT (PBE0/6-31G*) level, accounting for the contribution of the MM environment, whose coordinates were kept frozen. QM-MM interactions were

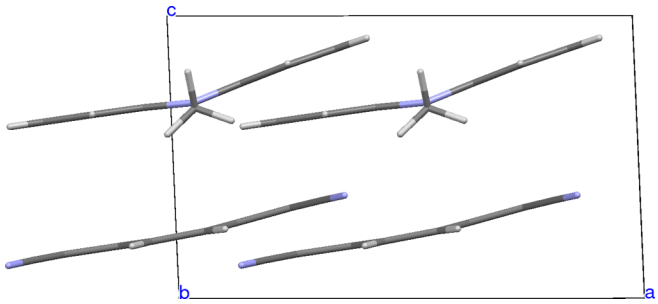

FIG. 1. Structure of M_2P-TCNQ viewed along the *b* crystal axis.

modelled with the point atomic charges (from electrostatic potential fitting of the DFT density) and van der Waals parameters taken from the GAFF 2010 force field [46].

III. RESULTS

A. Structural analysis

We solved the x-ray crystal structure at RT and 130 K, confirming earlier results [47], but with a better refinement factor: R1 = 0.0303 and 0.0226 at room T and 130 K. At RT M_2P-TCNQ crystallizes in the monoclinic system with $a = 11.1959(5)$ Å, $b = 13.5747(6)$ Å, $c = 6.7860(3)$ Å, and $\beta = 92.436(1)°$. Extinctions affecting the *hkl* reflections with $h + k = 2n$ indices point out C centering so that attempts to solve the structure were carried out in the three possible space groups of the corresponding Laue class. The centrosymmetric $C2/m$ and $C2$ space groups produced meaningless results, while the sole reliable solution was found in the polar space group Cm (C_s^3), $Z = 2$. Further details of the x-ray structure are reported in Table S1 of the Supplemental Material [45].

No phase transitions are detected by lowering T down to 130 K, and the structure retains its RT features, with a slight contraction of the *b* and *c* lattice parameters (0.67 and 1.46%, respectively) and a noteworthy increase of *a* of about 0.3%. No hints of structural disorder are detected, as small, regular, thermal ellipsoids are observed at both temperatures. On the other hand, crystals with polar point group symmetry usually present inversion twinning that we analyzed first by the Shelxl TWIN option. Both at RT and at 130 K the resulting Flack parameter [48] turns out to be far from the 0 and 1 values expected for untwinned structures. However, the estimates are affected by large uncertainties, likely related to the slight centrosymmetry breaking (i.e., deviation from planar geometry). A more refined symmetry analysis making use of Parsons' method [49] is less affected by uncertainty and yields values of 0.34(7)and 0.59(6) for the RT and 130 K data collections, respectively. Therefore all the available elements point to the presence of inversion twinning, although the scale of the twinned domains cannot be established.

Figure 1 depicts a projection of the structure viewed along the *b* crystal axis. M_2P appears significantly folded along the N-N line with a dihedral angle of about 167°, while TCNQ is also slightly bent. The dihedral angle of both molecules increases by about one degree upon going to low T. The two molecules alternate along the *c* axis forming a mixed stack

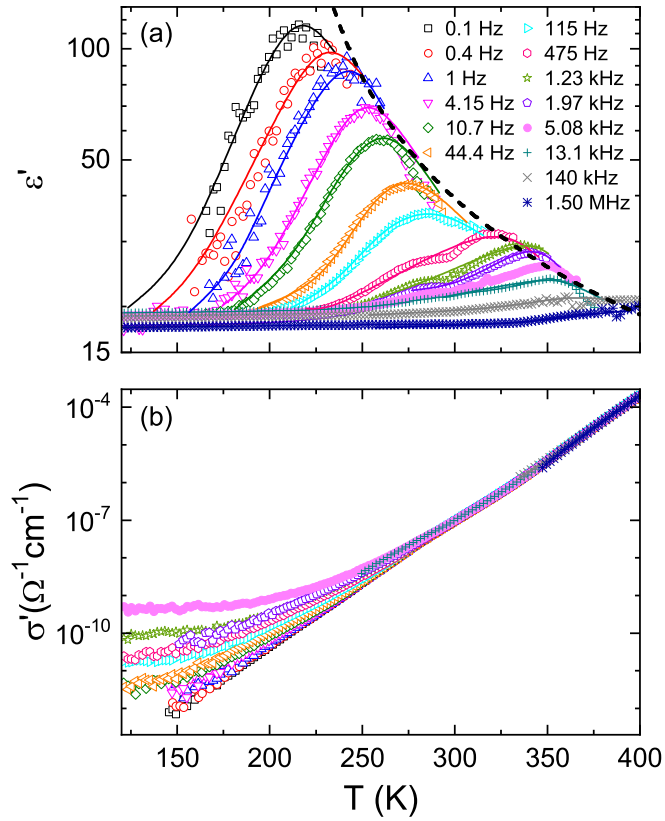

FIG. 2. (a) Temperature dependence of the real part of the dielectric constant $\varepsilon'(T)$. The solid lines are guides to the eyes, while the dashed line indicates Curie-Weiss behavior of the right flanks of the peaks, representing the static dielectric constant. (b) Temperature dependence of the conductivity $\sigma'(T)$.

where π-π and π-H interactions seem to dominate. Weak hydrogen bonds affect the interstack packing, involving the cyanide and methyl groups of TCNQ and M_2P, respectively, while at low T a slightly stronger network of interstack interactions sets in, also involving the TCNQ aromatic H atoms (see Fig. S1) [45]. The DA stacks are dimerized as obviously pointed out by the alternating distances between the molecular centroids $d_1 = 3.341$, $d_2 = 3.513$ Å at 300 K and $d_1 = 3.305$, $d_2 = 3.473$ Å at 130 K. The two stacks are dimerized in-phase, i.e., the system is polar, in agreement with the Cm point group symmetry of the crystal, allowing in principle the presence of a spontaneous electric polarization within the *ac* plane.

The TCNQ distances can be used to estimate the degree of CT or ionicity ρ [50], which turns out to be 0.44. This is less than the $\rho \sim 0.5$ deduced from IR spectra [27], but one has to keep in mind that the estimates by bond distances are not particularly accurate, especially for ρ appreciably different from zero and/or when the TCNQ is slightly distorted like in this structure. In any case x-ray diffraction demonstrates that in going to low T the ionicity does not change.

B. Dielectric measurements

Given its crystal structure, M_2P-TCNQ is a good candidate for FE. To detect polar behavior, dielectric spectroscopy, polarization, and PUND measurements in a wide frequency

and temperature range were performed, with the electric field aligned exactly parallel to the c stack axis, so that contributions along other directions are not detected. In Fig. 2(a) the temperature-dependent real part of the dielectric constant $\varepsilon'(T)$ between 0.1 Hz and 1.50 MHz is shown. Large peaks in the permittivity are observed, similar to the peaks at the ferroelectric transition in the related material M_2P-Dimethyl-TCNQ (M_2P-DMeTCNQ) [51]. The peaks decrease in amplitude and shift to higher temperatures with increasing frequency, which constitutes the typical relaxor FE behavior [52,53]. In the 0.1 Hz curve the dielectric constant at the peak temperature $T_p = 219$ K is slightly above 100. At frequencies in the kHz range, the peaks become less and less pronounced, being barely visible in the 13.1 kHz curve at $T_p = 357$ K with $\varepsilon'(T_p) \approx 20$. It should be noted that relaxor behavior is somewhat different from conventional dielectric relaxations, as it is characterized by a strongly increasing static susceptibility with decreasing temperature, which leads to the typical peaks in the $\varepsilon'(T)$ curves [Fig. 2(a)] not expected in conventional relaxations.

To check if the observed relaxorlike behavior of $\varepsilon'(T)$ is intrinsic and not a contact-related artifact [54], several samples were investigated. Some of the samples were measured with gold paint contacts (flake sizes $\lesssim 10$ μm), others with carbon paste (average flake sizes $\simeq 1$ μm) (see Fig. S2 and S3 of the Supplemental Material [45]). It is indeed well known that the grain size of the metal particles in the paste plays a large role for the formation of Schottky diodes. Therefore, the different contact materials used here, and especially their differing particle sizes, would lead to different results if the relaxor behavior were extrinsic. Additionally, the samples also feature different area-to-thickness ratios, which would lead to marked differences in the dielectric response of space-charge effects but not in the intrinsic behavior of the system [54]. All investigated samples do in fact exhibit very similar relaxorlike behavior, thus indicating that the origin of relaxor ferroelectricity in M_2P-TCNQ is intrinsic.

Due to the needlelike geometry, the electrode area and thus the measured capacitance are very small leading to a large uncertainty of the absolute values of ε'. By comparing different measurements, we obtain a rough estimate for the value of the high frequency dielectric constant $\varepsilon_\infty \approx 10$, or somewhat above. Such a value is indicative of a relatively high polarizability, as we shall discuss in more detail in Sec. III E. Note that at about 300 K a small anomaly of unknown origin is observed at several frequencies, e.g., in the 475 Hz curve, it was also found in the other samples. Finally, the dashed line in Fig. 2(a) is a Curie-Weiss fit to the right flanks of the relaxor peaks, representing the static dielectric constant, with a Curie-Weiss temperature of $T_{CW} \approx 206$ K, which provides an estimate of the quasistatic freezing temperature.

Figure 2(b) shows M_2P-TCNQ's T-dependent conductivity $\sigma'(T)$. At 400 K $\sigma' \approx 2 \times 10^{-4}$ Ω^{-1} cm^{-1} is for all frequencies. With decreasing temperature, the conductivity decreases to about 10^{-7} Ω^{-1} cm^{-1} at room temperature. Below around 200 K the conductivity becomes slightly frequency dependent pointing to hopping charge transport [55,56] whose further investigation is outside of the scope of the present work. At 150 K the conductivity lies between 10^{-9} Ω^{-1} cm^{-1} and 10^{-12} Ω^{-1} cm^{-1}. The lowest frequency (0.1 Hz) value can be considered to correspond to the dc conductivity of M_2P-TCNQ, and indeed the value at 150 K, 7×10^{-12} Ω^{-1} cm^{-1}, is consistent with the value reported for a compacted polycrystalline sample, 10^{-11} Ω^{-1} cm^{-1} [57].

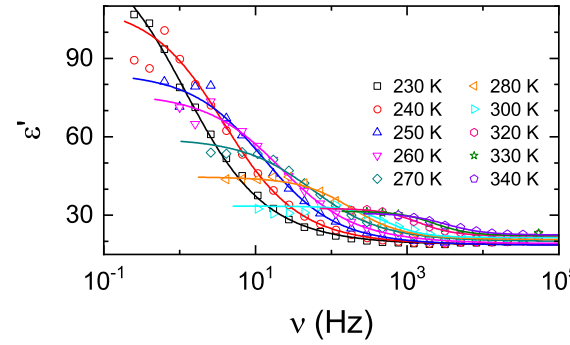

FIG. 3. Frequency-dependent plot of the dielectric constant $\varepsilon'(\nu)$ of M_2P-TCNQ at various temperatures, revealing a steplike decrease which shifts to lower frequencies with decreasing temperature. Lines are fits to the data with the phenomenological Cole-Cole equation.

A frequency-dependent plot of the dielectric constant $\varepsilon'(\nu)$ is shown in Fig. 3. The spectra reveal a steplike decrease of $\varepsilon'(\nu)$ which shifts to lower frequencies with decreasing temperature. This evidences the slowing down of relaxational dynamics with decreasing temperature. Similar to the peaks in $\varepsilon'(T)$, the height of curves in $\varepsilon'(\nu)$ decrease with increasing temperature, typical for relaxor ferroelectrics [52,53]. In the 230 K curve the highest value of $\varepsilon'(\nu)$ is 110, decreasing to about 30 in the 340 K curve. The lines shown here are fits to the data with the phenomenological Cole-Cole equation [58]. Both real and imaginary part were fitted at the same time, although the latter is strongly dominated by conductivity and the contribution from the relaxation process is minuscule. As can be seen from the data, $\Delta\varepsilon$ decreases with increasing temperature. The symmetric broadening parameter α decreases with temperature from 0.4 at 230 K to 0.1 at 320 K, while $\varepsilon_\infty \approx 20$ varies only slightly.

To further analyze the relaxor ferroelectricity, the peak temperatures in $\varepsilon'(T)$ were plotted in an Arrhenius representation, Fig. 4. A fit to the data (red line) with the linear Arrhenius equation [59] yields an activation energy $E_a \approx 0.52$ eV and a pre-exponential factor $\tau_0 = 1.9 \times 10^{-12}$ s. An independent analysis of the points of inflection in the frequency-dependent plot of the dielectric constant $\varepsilon'(\nu)$ in Fig. 3 yields very similar results (both when determined by eye and through fitting the data). Although the temperature evolution of the relaxation time of most relaxor ferroelectrics can be described by the Vogel-Fulcher-Tammann law [60–62], some relaxors, e.g., PLZT8/65/35 and SBN75 [63], follow Arrhenius behavior [59].

Polarization measurements performed on several samples of M_2P-TCNQ did not yield a ferroelectric response. The voltage was varied from 20 V to 1000 V (fields up to 50 kV/cm) and the frequency from 0.1 Hz to 1000 Hz at temperatures between 5 K and 270 K. Examples are shown in Fig. 5. At 5 K (upper frame), a nearly linear P-E behavior is observed. At the higher temperature of 155 K, the larger conductivity leads to an ellipsis, typical for a sample with

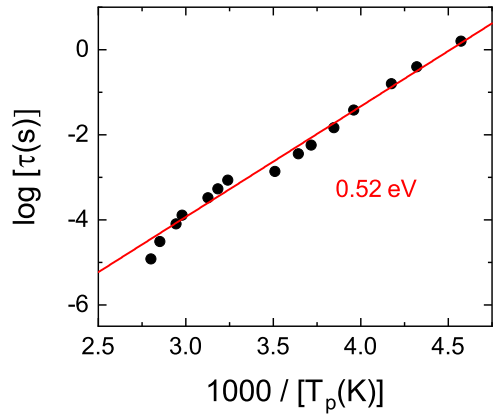

FIG. 4. Temperature evolution of M_2P-TCNQ's relaxation time in an Arrhenius plot. Fitting with the linear Arrhenius equation ($\tau = \tau_0 \exp[E_a/(k_B T)]$) yields an activation energy of $E_a \approx 0.52$ eV and a pre-exponential factor $\tau_0 = 1.9 \times 10^{-12}$ s.

some conductivity-related loss. Therefore, we detect well-pronounced polar dynamics, but no ferroelectric hysteresis. It seems likely that at 5 K, far below the relaxor peaks, the permanent dipoles are essentially frozen-in and cannot be polarized anymore. On the other hand, at higher temperatures the detection of the polarization is hampered by the dominating conductivity contribution. This is a common problem for ferroelectrics that are not perfect insulators.

We also tested polarization dynamics through PUND measurements. Under properly chosen conditions, they exhibit a quite unusual behavior, as shown in Fig. 6. The conditions used here are an electric field of 50 kV/cm, a frequency of 0.166 Hz, a temperature of 200 K, and a very short interval between pulses of 1 ms (not discernible in Fig. 6). These

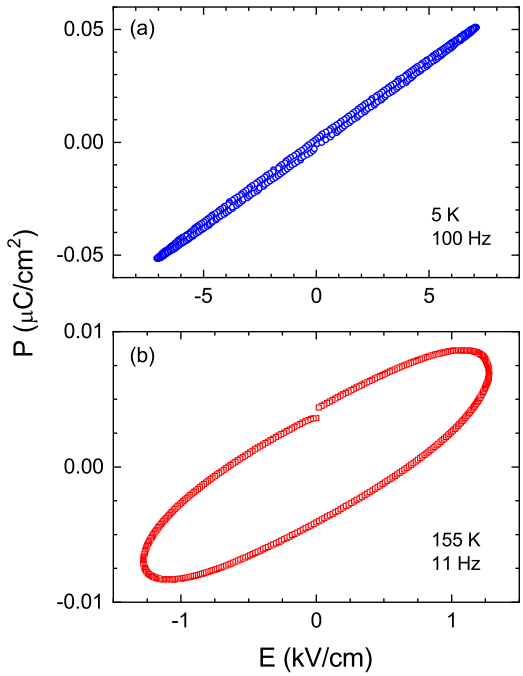

FIG. 5. Examples of polarization curves of M_2P-TCNQ at (a) 5 K and 100 Hz and (b) at 155 K and 11 Hz.

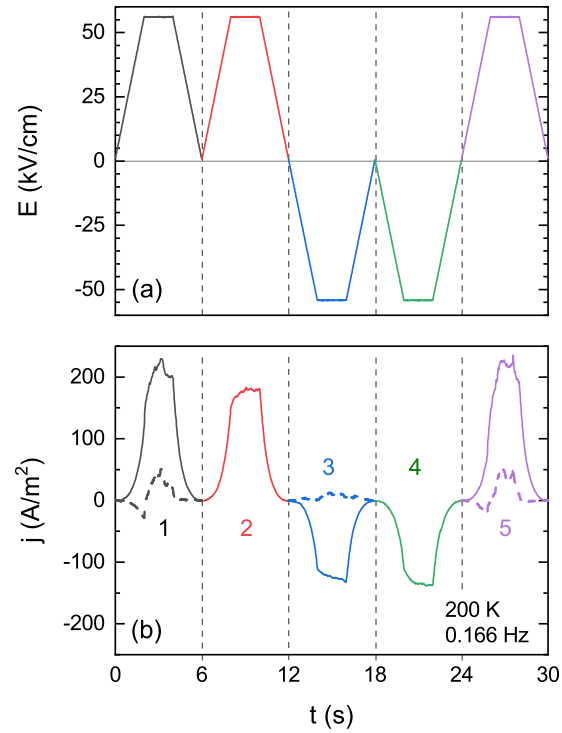

FIG. 6. Positive-up-negative-down (PUND) measurement of M_2P-TCNQ with (a) applied electric fields E of 50 kV/cm resulting in (b) current density pulses $j = I/A$ ($A = 0.0625$ mm^2), of which 1 and 5 are larger than 2. The negative pulses, 3 and 4, are virtually identical and smaller than the positive ones. The dashed lines show the differential current density (i.e., 2 subtracted from 1 and 5, and 3 subtracted from 4). Measured at a frequency of 0.166 Hz, a temperature of 200 K, and with a very short interval between pulses of 1 ms.

measurement conditions were chosen on the basis of dielectric data shown in Fig. 2. In order for the conductivity to be small the temperature should be as low as possible. At the same time measuring at a temperature only slightly below the dielectric peak in the spectrum is desirable, since there the ferroelectric correlations of the dipoles can be assumed to be high and the dipoles are sufficiently mobile to be polarizable by an external field. Therefore frequencies below 1 Hz and temperatures below 230 K are the most suitable choice. In PUND measurements the response of a ferroelectric is expected to feature an additional current contribution for the first of two successive pulses in the same direction (1,3,5), while the second pulse (2,4) is expected to be smaller. This reflects the fact that, after the first pulse, most dipoles are already oriented in field direction and, thus, the second successive pulse does not induce further dipolar motion. PUND measurements can in principle also be used to evidence ferroelectric behavior in rather conductive materials, where conventional $P(E)$ hysteresis measurements might not be possible (see, for example, Ref. [34]). As indeed observed in Fig. 6(b), the sample conductivity then should lead to a continuous increase and decrease of the current I (and thus current density j), following the increase and decrease of the field during the applied pulses. This should be superimposed by the polarization-induced current for the first pulse in each direction only. Such

an additional contribution is indeed seen in our experiments. In M_2P-TCNQ the positive first and fifth current pulses are, as expected, significantly larger than the second one. This can be clearly seen in the differential current density, where the polarization switching contribution (dashed lines in Fig. 6(b)) is revealed by subtracting the non-switching contributions (2 and 4) from the pulses that contain a switching contribution (1/5 and 3, respectively). It is further confirmed by calculating the time-integrated current, revealing that the area of peak 2 is about 9% smaller than those of peak 1 and 5. However, when applying a negative voltage, both pulses (3 and 4) are virtually identical and the current is about 30% smaller than in positive direction. The quantitative values of the PUND and dielectric measurements are unreliable due to the needlelike shape of the samples. They should therefore be seen as qualitative indications rather than exact determinations of the polarization value.

The just described asymmetric PUND behavior of M_2P-TCNQ is, to the best of our knowledge, unique. We remark that while we observed similar PUND pattern in another sample, some sample-to-sample difference is present. Due to the small sample cross section, the current density is unusually large. Although the peaks in positive direction resemble the typical response of a ferroelectric in PUND, the large current density might indicate an external cause. The observation of the properties depicted in Fig. 6 indeed require carefully chosen measuring conditions, with the employment of large electric fields of at least 50 kV/cm over several seconds. Higher fields of 60 kV/cm lead to breaking of the samples. This breaking could be caused simply by an electric breakdown, but on the other hand it may be an indication that full polarization switching is impeded by the molecular geometry of M_2P.

We offer the following plausible but somewhat speculative interpretation: the asymmetry is indicative of preferential one-directional polarization switching, since the bending of the M_2P can not easily be reversed due to interstack interactions. Forcing the reversal with very large fields involves strong crystallographic rearrangement that breaks the crystal. Our measurements cannot reveal whether this preferential direction is intrinsic to the crystal or determined by the poling history of the sample. Obviously, the dielectric processes in M_2P-TCNQ are relatively slow, compared to what would be expected of purely electronic switching [21]. However, we propose that the rearrangement of the electrons in turn leads to a deformation of the M_2P molecules, which slows down the process considerably. This would constitute the reverse of the situation in the $(TMTTF)_2X$ salts, where a rigid displacement of the anion chain leads to a shift of the electron holes on the donors [14].

C. Optical spectra

Optical spectra are a useful complement to structural and dielectric data, so we verified and extended early spectroscopic data [27]. The spectra reported in the Supplemental Material [45] confirm that the M_2P-TCNQ degree of ionicity ρ is ~0.5, with the CT transition occurring around 5050 cm^{-1} or 0.63 eV. We also recorded the IR and Raman spectra as a function of T, from 430 to 80 K. The T evolution of the

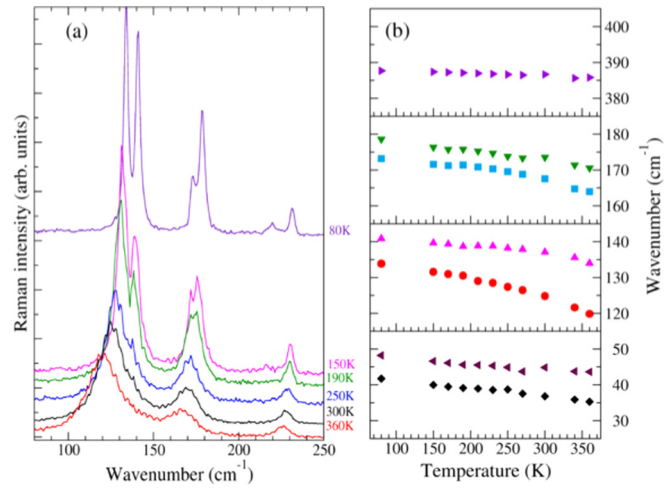

FIG. 7. (a) Low-frequency Raman spectra of M_2P-TCNQ, (c, c) polarization, as a function of temperature, exciting line: 752 nm and (b) Temperature evolution of the frequencies of selected bands.

spectra in the region of the molecular vibrations shown in Fig. S5 and S6 [45] demonstrate that in this temperature interval there is no phase transition and that the ionicity or the extent of dimerization do not change appreciably, in agreement with X-ray and DSC analysis [57]. New relevant information is instead obtained from the Raman spectra in the lattice (intermolecular) phonon region (30–200 cm^{-1}) shown in Figs. 7 and 8.

Fig. 7(a) reports the T evolution of M_2P-TCNQ low-frequency Raman spectra with polarization (c, c), i.e., incident and scattered radiation with the electric vector parallel to the stack. At room T (black trace in Fig. 7) the spectra are dominated by two broad bands around 125 and 170 cm^{-1} . By increasing the temperature the bands soften and become broader (bandwidth ≈35 cm^{-1} at 430 K). By lowering T, they narrow considerably and become clearly separated into two bands between 200 and 150 K. To follow the temperature dependence of the frequencies of these two pairs of bands, we performed a spectral deconvolution in terms of Voigt profiles, starting from the lowest temperature where all the bands are clearly resolved. Examples of the deconvolution are reported in Fig. S7 of the Supplemental Material [45]. A stable fitting is found up to 360 K, beyond which the bands become too broad to give confidence to the result. The central panels of Fig. 7(b) shows the temperature evolution of the frequencies of the four bands, evidencing a considerable frequency softening (15–20 cm^{-1}) by increasing T in the explored temperature range, a fact pointing to a strong degree of anharmonicity for the associated phonons. The softening of the other low-frequency phonons is indeed less pronounced (top and bottom right panels of the Figure) and corresponds to what is normally expected due to thermal expansion.

The anharmonicity of the four phonon modes associated with the two pairs of bands around 125 and 170 cm^{-1} is likely due to a strong electron-phonon coupling [64]. This idea is confirmed by the collection of spectra with different excitation lines, shown in Fig. 8. It is seen that by shifting the exciting line towards longer wavelengths, namely, by going closer to the CT transition, the intensity of the 125 and 170 cm^{-1}

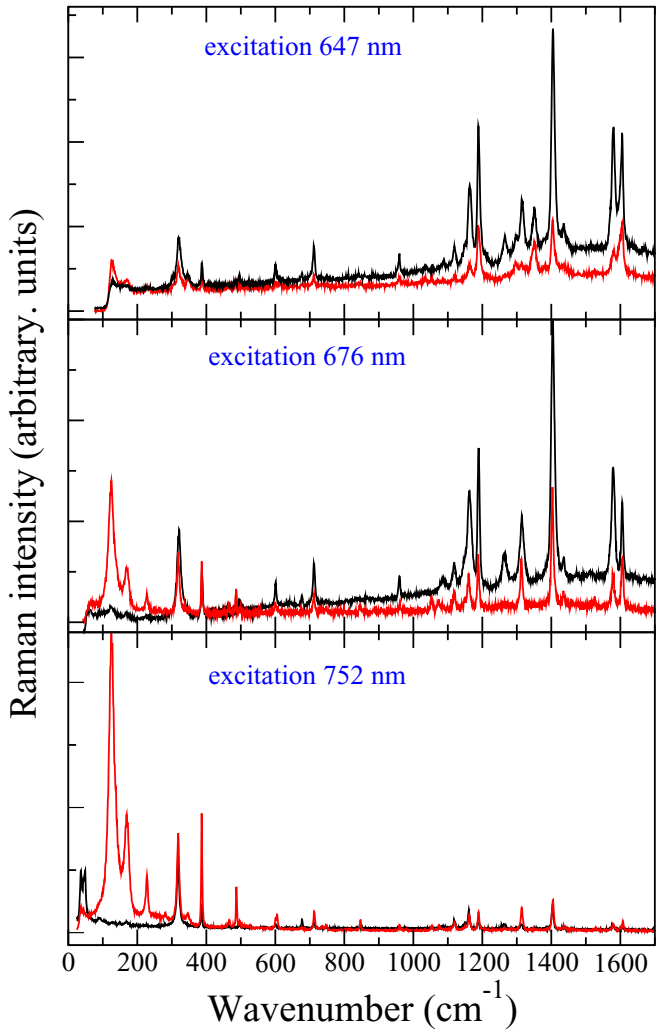

FIG. 8. M_2P-TCNQ polarized Raman spectra recorded with different exciting lines, $T = 300$ K. Red line: (c, c) polarization; Black line: $(\perp c, \perp c)$ polarization.

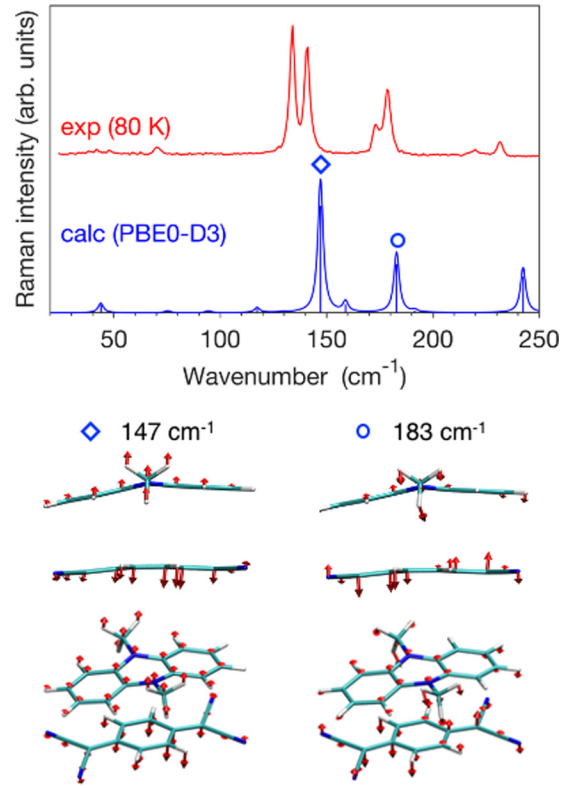

FIG. 9. Experimental (752 nm excitation) and calculated low-frequency Raman spectrum of M_2P-TCNQ, (cc) polarization. The eigenvectors of the two most intense Raman bands, corresponding to the prominent experimentally observed bands, are shown at the bottom.

groups of bands is strongly enhanced with respect to that of the other ones, also in the different polarization. This resonance intensity enhancement is known to be a consequence of the electron-phonon coupling [65].

To properly interpret the lattice phonon spectrum and to gain additional insight into the electron-phonon coupling mechanism, we performed DFT calculations of M_2P-TCNQ intermolecular phonons. The experimental and calculated spectrum are compared in Fig. 9.

The agreement between experiment and calculation can be considered satisfactory, having in mind that the experiment is done in pre-resonance with the CT transition, whereas the calculated Raman intensities are for off-resonance spectra. It is natural to associate the pair of bands calculated at 147–159 cm^{-1} and 183–192 cm^{-1} with the experimental pairs 134–141 cm^{-1} and 173–179 cm^{-1} (at 80 K). The eigenvectors of the two pairs are mixed, given the proximity of their frequency, but in any case the lowest frequency pair is mainly associated with the dimerization mode (relative displacement of the two sublattices along the stack direction), and the highest frequency one with the "butterfly" motion of M_2P, as illustrated in the lower part of Fig. 9. Both these motions are involved in a hypothetical high temperature phase transition towards a paraelectric phase [66]. As such, they are expected to be strongly coupled to the electronic CT system, determining the strong anharmonicity that was detected experimentally.

D. First principles calculations

DFT calculations were performed in order to clarify the mechanism underlying the electrical polarization and its possible switching. Band structure calculations describe M_2P-TCNQ as a band insulator with direct bandgap [67] at the Γ point, and intermediate ionicity.

The stack dimerization of M_2P-TCNQ is intertwined with the folding of the M_2P molecule along the axis passing though the two central N atoms. Calculations of the equilibrium geometry in gas phase [45] demonstrate that the M_2P folding depends on the molecular charge, getting more planar upon positively charging. The M_2P^+ cation presents a "folding angle" of 163°, very similar to the value measured in the M_2P-TCNQ crystal where the molecular charge is ∼0.5. Molecular geometries may be strongly affected by intermolecular interactions in the solid state, especially in the presence of soft degrees of freedom as in the case of M_2P. Interestingly, fully ionic M_2P can be planar, as seen in the M_2P-$TCNQF_4$ CT crystal [68].

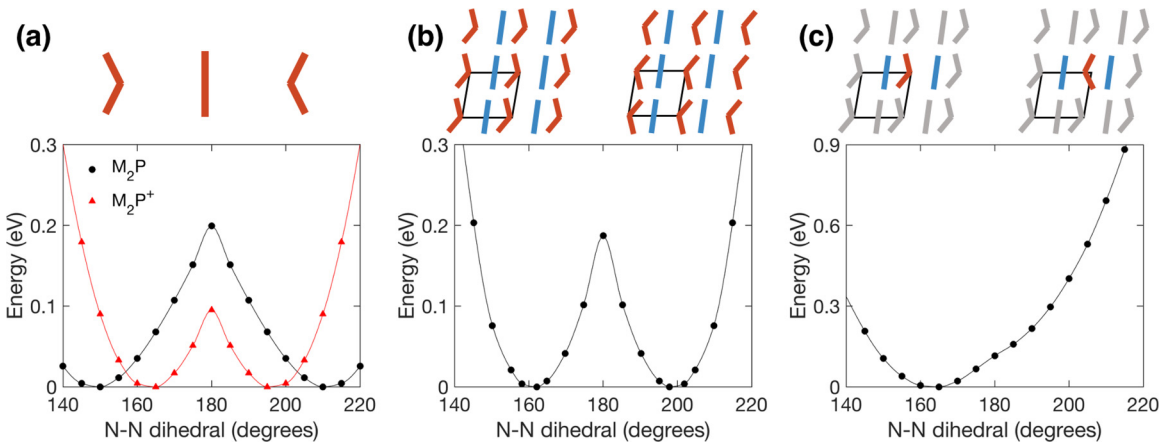

FIG. 10. Energy profile to invert the v-like conformation of M_2P (a) in the gas phase and (b),(c) in the crystal. Results from relaxed scans with a constraint on the dihedral angle connecting the two N atoms of M_2P. The upper sketches (M_2P in red, TCNQ in blue) illustrate the flipping procedure. (b) Energy scan to simultaneously flip all M_2P molecules in the crystal obtained with periodic DFT calculations. (c) Energy scan to flip one M_2P molecules in the crystal from QM/MM calculations. The central M_2P molecule and the two neighboring TCNQ along the stack were relaxed at the DFT level, in the field of the other molecules in the crystal (gray molecules in the sketch) that were kept frozen and described with point charges and Lennard-Jones potential. Lines are guides to the eyes.

The considerations above imply that polarization switching would require not only the change in the direction of dimerization but also the flipping of the M_2P conformation. This is specific to this CT crystal with v-shaped molecules that has no counterpart in more common systems (e.g., TTF-CA) featuring molecules that are planar in the gas phase and only exhibit small deviations from planarity in the crystal. This difference is likely to affect the mechanism of polarization reversal, being a possible origin of the relaxor and unique PUND behavior.

We hence calculated the energy profile for flipping the molecule in the gas phase and in the crystal—see Fig. 10. The results for an isolated M_2P, shown in (a), illustrate that the molecular charge affects both the equilibrium geometry (as discussed above, see Fig. S8 [45]) and also the energy barrier required to flip the molecule. The barrier for M_2P of 0.2 eV is approximately double that of the cation. A barrier of 0.2 eV was also obtained with periodic DFT calculations for the M_2P-TCNQ crystal, as shown in Fig. 10(b). This corresponds to the energy barrier to invert the polarization in a single-domain macroscopic crystal. We note that since this barrier is much larger than the room-temperature thermal energy (26 meV), the polarization reversal appears to be energetically impeded. On the other hand, the barrier is comparable in magnitude with, yet significantly smaller than, the 0.5 eV estimated from the Arrhenius fit of the dielectric data depicted in Fig. 4 (Sec. III B).

We also considered a third possibility, in which a single M_2P molecule is flipped in the crystal that retains the original polarization—see Fig. 10(c). This situation corresponds to the creation of a defect in the otherwise periodic crystal structure and was modelled with hybrid quantum/classical calculations (QM/MM, see Methods). In this case, the only stable configuration remaining is that with all M_2P molecules pointing in the same direction, since the second conformation is strongly destabilized by intermolecular interactions in the solid. Such a destabilization is imputable to dispersion interactions and steric repulsion and not to an electrostatic effect associated with the dipole reversal on the central molecule. Indeed, a similar energy profile is obtained by neglecting electrostatic interactions with the MM environment.

As stated above, polarization inversion requires both the inversion of the dimerization and the flipping of M_2P. We may expect that phonons associated with those motions are the most strongly coupled to the electronic CT system, hence the most anharmonic, identified experimentally with the two groups of bands around 125 and 170 cm^{-1} (room T frequencies).

The bent shape of M_2P also has important consequences on the amplitude of dimerization of the mixed stack. In the context of lattice models for the electronic structure, the dimerization amplitude is usually defined as $\delta = (t_1 - t_2)/(t_1 + t_2)$, where t_1 and t_2 are the charge transfer integrals between neighboring donor and acceptor molecules along the stack. The two limiting cases $\delta = 0$ and $\delta = 1$ correspond to a regular stack of equally spaced molecules and to a crystal of nonoverlapping dimers, respectively. We obtain $t = (t_1 + t_2)/2 = 493$ meV and $\delta = 0.32$ [69]. On the other hand, it is known that the magnitude of transfer integrals in donor-acceptor complexes strongly depends on the functional employed [70], whereas the value of the dimerization amplitude $\delta = 0.32$ is weakly functional dependent. This δ value for M_2P-TCNQ is considerably larger than that calculated for the ionic phase of TTF-CA at the same level of theory, $\delta = 0.19$. This remarkable difference between the two systems suggests that M_2P-TCNQ, owing to its nonplanar shape of the donor molecule, is more suited to be described as a collection of weakly overlapping dimers.

We then calculated the electric polarization of the M_2P-TCNQ crystal (Fig. S9 [45]). These calculations aim at predicting the **P** that one would measure if it were possible to switch the polarization as in a normal ferroelectric phase, such as in TTF-CA [15]. The data in Table I reveal that the polarization of M_2P-TCNQ has two components along a and c that are

TABLE I. Components of M_2P-TCNQ electrical polarization **P** calculated with periodic DFT and with classical models. DFT results include both electronic (Berry phase) and nuclear contributions. The table reports the components along the *a* and *c* crystal axes (forming an angle of 92°). The polarization along *b* is zero by symmetry.

Model	P_a (μC/cm^2)	P_c (μC/cm^2)
PBE0	−5.88	−5.16
ionic	−0.87	0.04
dipolar	−0.02	0.40

comparable in magnitude. This surprising result reveals another intriguing difference with respect to other mixed stacks with planar molecules (TTF-CA, TTF-QBrCl$_3$, TTF-BA), for which the polarization is essentially directed along the stack axis [16]. In order to understand the physical origin of the polarization, Table I also reports the ionic polarization (calculated considering charges $\pm 0.5e$ at the molecular centroids, as in Ref. [15]) and the dipolar polarization. The latter accounts for the contribution of the dipole moments of the individual neutral molecules at the crystal structure geometry, calculated with gas-phase DFT. Ionic and dipolar contributions are both automatically included in the DFT calculation of the total polarization.

The stack-axis component of the polarization, $|P_c| = 5.16\ \mu\text{C/cm}^2$, is similar to what was measured for the ionic low-T phase of TTF-CA. The ionic polarization P_c is two orders of magnitude smaller that the total polarization and points in the opposite direction, marking an important analogy with TTF-CA and TTF-QBrCl$_3$ [71]. These similarities concerning the stack-axis polarization point to a common electronic mechanism of polarization, governed by fluctuations of electronic charges along the stack, rather than by the frozen ionic charges localized at molecular sites in a dimerized lattice. The dipolar contribution along *c* is non-negligible, allowing us to obtain an estimate of the electronic polarization by subtraction, $P_c^{(\text{el})} = P_c - P_c^{(\text{ion})} - P_c^{(\text{dip})} = -5.6\ \mu\text{C/cm}^2$.

As anticipated, the leading component P_a has no counterpart in traditional mixed-stack crystals. In this case the ionic and total polarization are parallel, with the former accounting for 15% of the total one. The ionic contribution along *a* is much larger in magnitude than its component parallel to *c*. This results from a more pronounced displacement of the donor and acceptor sublattices (with respect to a centrosymmetric arrangement) along *a* that can be also inferred from the visual inspection of the crystal structure in Fig. 1. Along *a* the dipolar contribution is negligible, leading to an electronic polarization $P_a^{(\text{el})} = -5.0\ \mu\text{C/cm}^2$, slightly smaller than $P_c^{(\text{el})}$. The physical origin of the surprisingly large electronic polarization along *a* is presumably connected to the bent shape of M_2P and with the just mentioned offset of its barycenter with respect to TCNQ, assisted by the interstack weak hydrogen bonding network (cf. Figs. 1 and S1). Despite our attempts [45], the precise origin of this unusual behavior remains elusive. On the other hand, with the M_2P-TCNQ needlelike crystals the polarization could only be measured along the *c* stack axis, and we prefer to simply report the calculation prediction along *a*, without investigating any further here.

Finally, we calculated the molecular polarizabilities at the PBE0/ma-def2-TZVP level and obtained $\alpha \approx 60$ Å^3 for either neutral molecules, $\alpha(M_2P) + \alpha(\text{TCNQ})$, or molecular ions, $\alpha(M_2P^+) + \alpha(\text{TCNQ}^-)$. The calculated polarizability of a dimer taken from the crystal structure is $\alpha(M_2P^{+\rho}\text{TCNQ}^{-\rho}) \sim 120$ Å^3 with $\rho = 0.44$ close to the experimental $\rho \sim 0.5$. Since molecular polarizabilities are too small to account for the $\varepsilon_\infty \approx 20$ value in Sec. III B, we consider polarizability due to the crystalline environment.

E. A simple model for strongly dimerized mixed stacks

The first principles calculations of the previous subsection put in evidence the prevailing electronic origin of the polarization of the M_2P-TCNQ crystal. Electronic FE requires a highly polarizable lattice. Here we focus on the microscopic origin of the high polarization through a simple semiempirical model. The reference model for the electronic structure of ms-CT crystals is a Peierls-Hubbard model with staggered site energies for donor (D) and acceptor (A) sites and long-range Coulomb interactions [72]. The large dimerization of M_2P-TCNQ stacks, however, suggests that a first approximation to the crystal described is nonoverlapping donor-acceptor (D-A) dimers along the stack with 3D Coulomb interactions with all other dimers. The mean-field treatment of the interactions between dimers leads to the so-called embedded Mulliken dimer model that was introduced in Ref. [25] and recently reviewed [72].

The Mulliken dimer model describes an isolated dimer on the basis of neutral $|\text{DA}\rangle$ and ionic $|\text{D}^+\text{A}^-\rangle$ electronic states. The Hamiltonian in the singlet sector reads:

$$H_0 = 2z_0\hat{\rho} - \sqrt{2}t\hat{\sigma}_x, \tag{1}$$

where $2z_0 = (\mathcal{I} - \mathcal{A} - V)$, $\mathcal{I}$ is the D ionization potential, $\mathcal{A}$ is the A electron affinity, V is the nearest neighbor Coulomb interaction, and t is the CT integral. $\hat{\rho} = (1 - \hat{\sigma}_z)/2$ is the ionicity operator, where $\hat{\sigma}_z$ and $\hat{\sigma}_x$ are the Pauli matrices. Having defined the dipole moment operator as $\hat{\mu} = ea\hat{\rho}$, where e is the electron charge and $a = 3.5$ Å is the intermolecular spacing, the polarizability of the isolated dimer can be expressed in terms of the ground state ionicity:

$$\alpha_0(\rho) = \frac{2(ea)^2}{\sqrt{2}t}(\rho(1-\rho))^{3/2}. \tag{2}$$

The Hamiltonian for an embedded dimer is formally equivalent to Eq. (1) with z_0 replaced by $z = z_0 - \epsilon_c\rho$, where

$$\epsilon_c = M - V, \tag{3}$$

and M is the Madelung energy of the ionic ($\rho = 1$) lattice. The embedded dimer Hamiltonian depends self-consistently on ρ, which accounts for cooperative interdimer interactions in the solid state. Positive ϵ_c values correspond to attractive interactions between dimers, favoring the ionic state. The model describes the crossover between a neutral and an ionic ground state upon decreasing $z(\rho)$. The crossover is continuous at $\rho = 0.5$ ($2z = \mathcal{I} - \mathcal{A} - V - \epsilon_c$) for $\epsilon_c < 2\sqrt{2}t$, while a first-order transition with a phase coexistence region is obtained

for $\epsilon_c > 2\sqrt{2}t$. The polarizability of the embedded dimer is

$$\alpha(\rho) = \frac{\alpha_0(\rho)}{1 - [2\epsilon_c\alpha_0(\rho)]/(ea)^2]}. \quad (4)$$

This self-consistent analytical result was previously obtained for an analogous Hamiltonian that describes the vibrational enhancement of the electric susceptibility of push-pull chromophores [73].

Equation (4) is general and together with Eq. (2) shows that the polarizability of the embedded dimer is maximum for intermediate $\rho \sim 1/2$ as in M_2P-TCNQ. Since $\rho(1-\rho) = 1/4 - (\rho - 1/2)^2$, we get

$$\alpha(0.5) = \frac{(ea)^2}{2[2\sqrt{2}t - (M-V)]}, \quad (5)$$

i.e., the polarizability from intermolecular CT degrees of freedom may become very large on approaching the critical point $(M-V) = 2\sqrt{2}t$, where it diverges.

In order to check the prediction of the model, we of course need to estimate the relevant parameters. According to the embedded dimer model, the energy of the CT transition for $\rho = 0.5$ is $E_{CT} = 2\sqrt{2}t$, so that $t \simeq 0.2$ eV. We followed the method described in Ref. [74] to calculate $\epsilon_c = M - V = 2.6 - 2.2$ eV $= 0.4$ eV. We are indeed relatively close to the critical point separating continuous from discontinuous crossover, and from Eq. (5) we get $\alpha \approx 800$ Å^3.

Always within the embedded dimer model, we can also estimate α from the experimental value of $\varepsilon_\infty \approx 20$ and the relation $\varepsilon_\infty = 1 + 4\pi\alpha/V_{DA}$, where $V_{DA} = 502$ Å^3 is the volume occupied by the DA dimer. We obtain $\alpha \approx 760$ Å^3, a value perfectly consistent with that derived from Eq. (5). Therefore, a major contribution to the dielectric response arises from intermolecular CT degrees of freedom, enhanced by solid-state electrostatic interactions. This simple treatment gives some general clues about the microscopic requirements to achieve highly polarizable electronic systems and hence promising candidates for electronic FE.

IV. DISCUSSION AND CONCLUSION

The performed dielectric measurements of M_2P-TCNQ, a polar mixed-stack charge transfer crystal, provide clear evidence for relaxor FE behavior already above room temperature (Fig. 2). The analysis of the temperature-dependent relaxation time, derived from the temperature dependence of the dielectric constant, reveals an Arrhenius behavior with an energy barrier of $E_a \simeq 0.52$ eV (Fig. 4). Even with an electric field up to 50 kV/cm, we did not observe polarization switching, while larger fields lead to the breaking of the crystal. Under carefully chosen measuring conditions, we detect a unique asymmetric PUND behavior (Fig. 6), where the positive pulses exhibit a behavior reminiscent of FE, while the negative pulses are significantly smaller.

Literature optical data [27], fully confirmed by the present ones, indicate that M_2P-TCNQ is among the rare crystals at the borderline between neutral and ionic ground state, with ionicity $\rho \sim 0.5$ that does not appreciably change with temperature from 400 to 80 K. Raman measurements in the low-frequency spectral region put in evidence the presence of two pairs of anharmonic phonons, around 150 and 180 cm^{-1}, likely coupled to the electronic system. DFT calculations demonstrate that these phonons involve the dimerization (Peierls) mode and the butterfly motion of the bent M_2P molecule. These modes are intertwined through the common interaction with the CT and would be involved in a hypothetical transition to a high-temperature paraelectric phase.

Polarization switching in M_2P-TCNQ requires the flipping of the M_2P molecule, which implies an energy barrier of 0.2 eV for the isolated molecule (DFT estimate), which, however, might differ significantly in the solid state as a result of intermolecular interactions. This marks an important qualitative difference with respect to the prototypical CT ferroelectric TTF-CA, for which the polarization reversal implies only the rigid translation of planar molecules. First principles calculations reveal that the electrical polarization of M_2P-TCNQ is of *quantum electronic* nature, as in TTF-CA [75]. The magnitude of the stack-axis component (5.2 μC/cm^2) is similar to the one measured for TTF-CA and TTF-QBrCl$_3$ [15]. Thus the possible ferroelectricity of M_2P-TCNQ is of *electronic origin* but does not constitute purely electronic *switching* due to the involvement of the bending M_2P molecule.

M_2P-TCNQ offers an intriguing and challenging experimental scenario, especially concerning the understanding of the relaxor behavior. Relaxor ferroelectricity is often associated with some kind of disorder [29]. In molecular salts disorder was introduced artificially in a controlled way [30], yet relaxor behavior was also observed in pristine systems, e.g., λ-(BEDT-TSF)$_2$FeCl$_4$ [31], κ-CN [32], and α-(ET)$_2$I$_3$ [34]. The absence of structural disorder in our samples does not exclude the possibility of disorder on a smaller scale, like charge defects or nanodomains with opposite dipolar orientation, as suggested by the intermediate value of the Flack parameter in the x-ray analysis. Another possible origin of relaxor behavior is the bent geometry of M_2P molecules, as shown in Fig. S8 [45].

Based on the available data, it seems plausible that the domain-wall motion under the action of an electric field is extremely slow in M_2P-TCNQ as compared to mixed-stack CT crystals of planar molecules, such as TTF-CA. The latter exhibits clean hysteresis loops [15] and full sample poling at fields of 0.95 kV/cm, after which the sizable contribution of domain walls (soliton) motion to the dielectric constant in the ionic phase is suppressed [76]. The bent shape of M_2P with its two stable conformations separated by a large energy barrier, which is probably enhanced by intermolecular interaction at the domain boundary, is likely to be the origin of the singular behavior of this material. We therefore expect that the relaxation dynamics associated with domain-wall motions depend on the specific features of the domain boundary and its interplay with structural defects, which may provide a rationale for the broad spectrum of characteristic timescales observed by dielectric spectroscopy. As a rare example of a ms-CT salt that is relaxor ferroelectric above room temperature, the details of M_2P-TCNQ's electronic ferroelectricity deserve further attention in future studies.

ACKNOWLEDGMENTS

We thank Prof. Anna Painelli for enlightening discussions. G.D. thanks Bartolomeo Civalleri for technical support with the CRYSTAL code. J.K.H.F. and P.L. acknowledge funding from the Deutsche Forschungsgemeinschaft (DFG) via the Transregional Collaborative Research Center TRR80 (Augsburg, Munich). J.K.H.F. was supported by JSPS [Postdoctoral Fellowships for Research in Japan (Standard)] as an International Research Fellow. In Parma the work has benefited from the equipment and support of the COMP-HUB Initiative, funded by the "Departments of Excellence" program of the Italian Ministry for Education, University and Research (MIUR, 2018-2022).

[1] Y. Tokura, S. Koshihara, Y. Iwasa, H. Okamoto, T. Komatsu, T. Koda, N. Iwasawa, and G. Saito, Phys. Rev. Lett. **63**, 2405 (1989).

[2] F. Nad, P. Monceau, and H. M. Yamamoto, J. Phys.: Condens. Matter **18**, L509 (2006).

[3] J. van den Brink and D. I. Khomskii, J. Phys.: Condens. Matter **20**, 434217 (2008).

[4] S. Horiuchi and Y. Tokura, Nat. Mater. **7**, 357 (2008).

[5] S. Tomić and M. Dressel, Rep. Prog. Phys. **78**, 096501 (2015).

[6] P. Lunkenheimer and A. Loidl, J. Phys.: Condens. Matter **27**, 373001 (2015).

[7] E. Gati, J. K. H. Fischer, P. Lunkenheimer, D. Zielke, S. Köhler, F. Kolb, H.-A. K. von Nidda, S. M. Winter, H. Schubert, J. A. Schlueter, H. O. Jeschke, R. Valentí, and M. Lang, Phys. Rev. Lett. **120**, 247601 (2018).

[8] P. Monceau, F. Y. Nad, and S. Brazovskii, Phys. Rev. Lett. **86**, 4080 (2001).

[9] F. Nad and P. Monceau, J. Phys. Soc. Jpn. **75**, 1 (2006).

[10] D. Starešinić, K. Biljaković, P. Lunkenheimer, and A. Loidl, Solid State Commun. **137**, 241 (2006).

[11] K. Yoshimi, H. Seo, S. Ishibashi, and S. E. Brown, Phys. Rev. Lett. **108**, 096402 (2012).

[12] G. Giovannetti, R. Nourafkan, G. Kotliar, and M. Capone, Phys. Rev. B **91**, 125130 (2015).

[13] M. Naka and S. Ishihara, Sci. Rep. **6**, 20781 (2016).

[14] J.-P. Pouget, P. Foury-Leylekian, P. Alemany, and E. Canadell, Phys. Status Solidi B **249**, 937 (2012).

[15] K. Kobayashi, S. Horiuchi, R. Kumai, F. Kagawa, Y. Murakami, and Y. Tokura, Phys. Rev. Lett. **108**, 237601 (2012).

[16] S. Horiuchi, K. Kobayashi, R. Kumai, and S. Ishibashi, Chem. Lett. **43**, 26 (2014).

[17] J. B. Torrance, J. E. Vazquez, J. J. Mayerle, and V. Y. Lee, Phys. Rev. Lett. **46**, 253 (1981).

[18] J. B. Torrance, A. Girlando, J. J. Mayerle, J. I. Crowley, V. Y. Lee, P. Batail, and S. J. LaPlaca, Phys. Rev. Lett. **47**, 1747 (1981).

[19] A. Girlando, F. Marzola, C. Pecile, and J. B. Torrance, J. Chem. Phys. **79**, 1075 (1983).

[20] M. Masino, N. Castagnetti, and A. Girlando, Crystals **7**, 108 (2017).

[21] T. Miyamoto, H. Yada, H. Yamakawa, and H. Okamoto, Nat. Commun. **4**, 2586 (2013).

[22] A. S. Tayi, A. K. Shveyd, A. C.-H. Sue, J. M. Szarko, B. S. Rolczynski, D. Cao, T. J. Kennedy, A. A. Sarjeant, C. L. Stern, W. F. Paxton, W. Wu, S. K. Dey, A. C. Fahrenbach, J. R. Guest, H. Mohseni, L. X. Chen, K. L. Wang, J. F. Stoddart, and S. I. Stupp, Nature (London) **488**, 485 (2012).

[23] G. D'Avino, M. Souto, M. Masino, J. K. H. Fischer, I. Ratera, X. Fontrodona, G. Giovannetti, M. J. Verstraete, A. Painelli, P. Lunkenheimer, J. Veciana, and A. Girlando, Nature (London) **547**, E9 (2017).

[24] Z. G. Soos, H. J. Keller, W. Moroni, and D. Nöthe, J. Am. Chem. Soc. **99**, 5040 (1977).

[25] Z. G. Soos, H. J. Keller, W. Moroni, and D. Nöthe, Ann. N.Y. Acad. Sci. **313**, 442 (1978).

[26] D. Nöthe, W. Moroni, H. J. Keller, Z. G. Soos, and S. Mazumdar, Solid State Commun. **26**, 713 (1978).

[27] M. Meneghetti, A. Girlando, and C. Pecile, J. Chem. Phys. **83**, 3134 (1985).

[28] A. A. Bokov and Z. G. Ye, J. Mater. Sci. **41**, 31 (2006).

[29] R. A. Cowley, S. N. Gvasaliya, S. G. Lushnikov, B. Roessli, and G. M. Rotaru, Adv. Phys. **60**, 229 (2011).

[30] S. Horiuchi, R. Kumai, Y. Okimoto, and Y. Tokura, Phys. Rev. Lett. **85**, 5210 (2000).

[31] H. Matsui, H. Tsuchiya, T. Suzuki, E. Negishi, and N. Toyota, Phys. Rev. B **68**, 155105 (2003).

[32] M. Abdel-Jawad, I. Terasaki, T. Sasaki, N. Yoneyama, N. Kobayashi, Y. Uesu, and C. Hotta, Phys. Rev. B **82**, 125119 (2010).

[33] S. Iguchi, S. Sasaki, N. Yoneyama, H. Taniguchi, T. Nishizaki, and T. Sasaki, Phys. Rev. B **87**, 075107 (2013).

[34] P. Lunkenheimer, B. Hartmann, M. Lang, J. Müller, D. Schweitzer, S. Krohns, and A. Loidl, Phys. Rev. B **91**, 245132 (2015).

[35] *APEX2, SAINT and SADABS* (Bruker AXS Inc., Madison, WI, 2008).

[36] M. Burla, R. Caliandro, B. Carrozzini, G. L. Cascarano, C. Cuocci, C. Giacovazzo, M. Mallamo, A. Mazzone, and G. Polidori, J. Appl. Crystallogr. **48**, 306 (2015).

[37] G. Sheldrick, Acta Crystallogr. C **71**, 3 (2015).

[38] R. Dovesi, A. Erba, R. Orlando, C. M. Zicovich-Wilson, B. Civalleri, L. Maschio, M. Rérat, S. Casassa, J. Baima, S. Salustro, and B. Kirtman, Wiley Interdiscip. Rev. Comput. Mol. Sci. **110**, e1360 (2018).

[39] F. Neese, Wiley Interdiscip. Rev. Comput. Mol. Sci. **2**, 73 (2011).

[40] F. Pascale, C. M. Zicovich-Wilson, F. L. Gejo, B. Civalleri, R. Orlando, and R. Dovesi, J. Comput. Chem. **25**, 888 (2004).

[41] S. Grimme, A. Hansen, J. G. Brandenburg, and C. Bannwarth, Chem. Rev. **116**, 5105 (2016).

[42] L. Maschio, B. Kirtman, M. Rérat, R. Orlando, and R. Dovesi, J. Chem. Phys. **139**, 164101 (2013).

[43] L. Maschio, B. Kirtman, M. Rérat, R. Orlando, and R. Dovesi, J. Chem. Phys. **139**, 164102 (2013).

[44] R. D. King-Smith and D. Vanderbilt, Phys. Rev. B **47**, 1651 (1993).

[45] See Supplemental Material at http://link.aps.org/supplemental/10.1103/PhysRevB.103.115104 for further details on x-ray, di-

electric, and IR/Raman measurements as well as first principles calculations.

[46] J. Wang, R. M. Wolf, J. W. Caldwell, P. A. Kollman, and D. A. Case, J. Comput. Chem. **25**, 1157 (2004).

[47] I. Goldberg and U. Shmueli, Acta Crystallogr., Sect. B **29**, 421 (1973).

[48] H. D. Flack, Acta Crystallogr., Sect. A **39**, 876 (1983).

[49] S. Parsons, H. D. Flack, and T. Wagner, Acta Crystallogr., Sect. B **69**, 249 (2013).

[50] P. Hu, K. Du, F. Wei, H. Jiang, and C. Kloc, Cryst. Growth Des. **16**, 3019 (2016).

[51] S. Horiuchi, R. Kumai, Y. Okimoto, and Y. Tokura, J. Am. Chem. Soc. **121**, 6757 (1999).

[52] L. E. Cross, Ferroelectrics **76**, 241 (1987).

[53] G. A. Samara, J. Phys.: Condens. Matter **15**, R367 (2003).

[54] P. Lunkenheimer, S. Krohns, S. Riegg, S. G. Ebbinghaus, A. Reller, and A. Loidl, European Physical Journal: Special Topics **180**, 61 (2010).

[55] A. R. Long, Adv. Phys. **31**, 553 (1982).

[56] S. R. Elliott, Adv. Phys. **36**, 135 (1987).

[57] I. Fujita and Y. Matsunaga, Bull. Chem. Soc. Jpn. **53**, 267 (1980).

[58] K. S. Cole and R. H. Cole, J. Chem. Phys. **9**, 341 (1941).

[59] S. Arrhenius, Z. Phys. Chem. **4**, S.226 (1889).

[60] H. Vogel, Physikalische Zeitschrift **22**, 645 (1921).

[61] G. S. Fulcher, J. Am. Ceram. Soc. **8**, 339 (1925).

[62] G. Tammann, Ann. Phys. **307**, 1 (1900).

[63] O. Kersten, A. Rost, and G. Schmidt, Phys. Status Solidi A **75**, 495 (1983).

[64] G. D'Avino, M. Masino, A. Girlando, and A. Painelli, Phys. Rev. B **83**, 161105(R) (2011).

[65] D. Pedron, A. Speghini, V. Mulloni, and R. Bozio, J. Chem. Phys. **103**, 2795 (1995).

[66] The transition is only hypothetical, since a rough estimate of the transition temperature T_P obtained by fitting one set of experimental soft frequencies [red dots in Fig. 7(b)] with the function $\omega = \omega_0\sqrt{T_P - T}$ yields $T_P \approx 1300$ K.

[67] The specific value of the gap markedly depends on the functional, varying between 0.53 eV for PBE (generalized gradient approximation), 0.83 eV for HSE06 (range-separated hybrid), and 1.32 eV for PBE0 (global hybrid).

[68] Z. G. Soos, H. J. Keller, K. Ludolf, J. Queckbörner, D. Wehe, and S. Flandrois, J. Chem. Phys. **74**, 5287 (1981).

[69] The calculations have been made at PBE0/6-31G* level, projective method [77], on M_2P-TCNQ dimers extracted from the crystal structure. The resulting average t is $t = (t_1 + t_2)/2 =$ 493 meV, and $\delta = 0.32$.

[70] G. Sini, J. S. Sears, and J.-L. Brédas, J. Chem. Theory Comput. **7**, 602 (2011).

[71] Note that the definition of electronic polarization adopted here is consistent with Ref. [15] and identifies the contribution of electronic charge flowing along the stack. Our ionic and electronic polarization do not refer to the contributions from core and valence charges, as customary for first principles calculations, cf. Refs. [75,78].

[72] G. D'Avino, A. Painelli, and Z. G. Soos, Crystals **7**, 144 (2017).

[73] A. Painelli, Chem. Phys. Lett. **285**, 352 (1998).

[74] F. Delchiaro, A. Girlando, A. Painelli, A. Bandyopadhyay, S. K. Pati, and G. D'Avino, Phys. Rev. B **98**, 199901(E) (2018).

[75] G. Giovannetti, S. Kumar, A. Stroppa, J. van den Brink, and S. Picozzi, Phys. Rev. Lett. **103**, 266401 (2009).

[76] F. Kagawa, S. Horiuchi, H. Matsui, R. Kumai, Y. Onose, T. Hasegawa, and Y. Tokura, Phys. Rev. Lett. **104**, 227602 (2010).

[77] E. F. Valeev, V. Coropceanu, D. A. da Silva Filho, S. Salman, and J.-L. Brédas, J. Am. Chem. Soc. **128**, 9882 (2006).

[78] S. Ishibashi and K. Terakura, Physica B Condens. Matter **405**, S338 (2010).

SUPPLEMENTAL MATERIAL

Intriguing relaxor behavior in a polar charge-transfer crystal at the neutral-ionic interface

J. K. H. Fischer, G. D'Avino, M. Masino, F. Mezzadri, P. Lunkenheimer, Z. G. Soos, and A. Girlando

Table of content

1. Details of the X-ray analysis

Table S1: refinement parameters and relevant structural data

Temperature	300 K	130 K
Crystal data		
space group	*Cm*	*Cm*
a (Å)	11.1959(5)	11.2322(5)
b(Å)	13.5747(6)	13.4837(6)
c (Å)	6.7860(3)	6.6870(3)
β (°)	92.4360(10)	92.4120(10)
V (Å^3)	1030.41(8)	1011.86(8)
Z	2	2
Radiation	Cu K_α	Cu K_α
μ (mm^{-1})	0.657	0.669
Data collection		
Diffractometer	Bruker *Venture*	Bruker *Venture*
Absorption correction	Multi-scan	Multi-scan
T_{min}, T_{max}	0.6579, 0.7247	0.6411, 0.7314
Indep./obs. [I > 2σ(*I*)] reflections	1679/1679	1869/ 1864
R_{int}	0.0141	0.0158
$(\sin \theta/\lambda)_{max}$ (Å^{-1})	0.619	0.626
Refinement		
$R[F^2]$, $wR(F^2)$	0.0303, 0.0856	0.0266, 0.0753
S	1.087	1.079
reflections	10073	9929
parameters	153	153
restraints	2	2
Geometry		
Stacking distance M2P-TCNQ (Å)	3.513	3.473
Stacking distance TCNQ-M2P (Å)	3.341	3.305
Dihedral angle M2P (°)	166.55	164.92
Dihedral angle TCNQ (°)	173.97	172.98

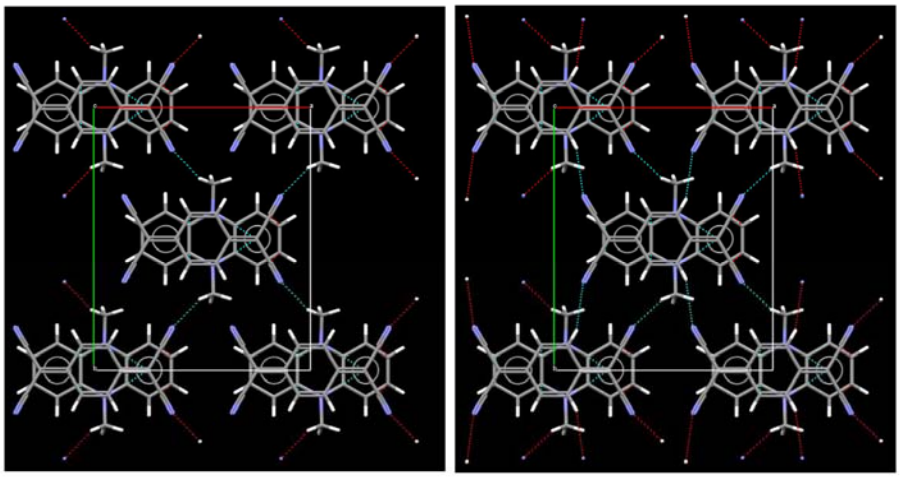

RT 130K

Figure S1. *Short contacts scheme at RT and 130 K*

2. Photographs of M_2P-TCNQ crystals with contacts for dielectric measurements

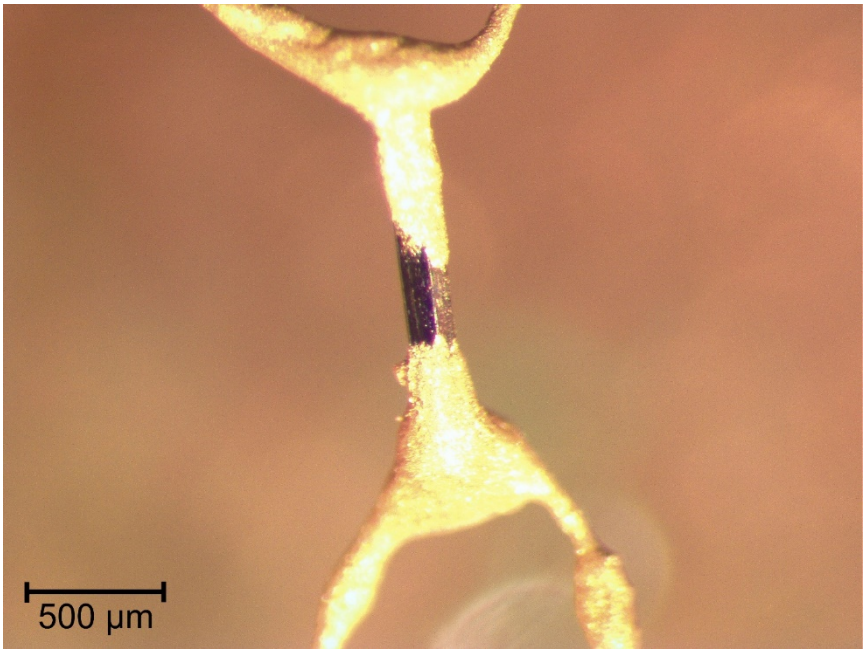

Figure S2. *A typical rod-like single crystal sample of M_2P-TCNQ attached to gold wires with electrodes of gold paint (flake sizes of <10 µm). The long crystal dimension is the stacking axis (c).*

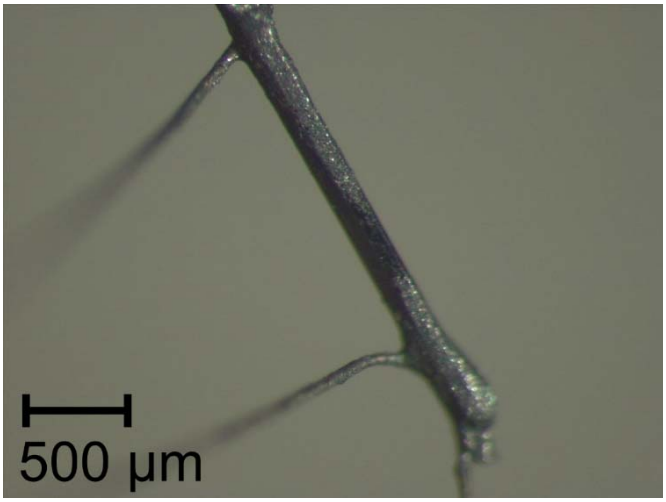

Figure S3. *Picture of a black M_2P-TCNQ sample attached to gold wires with electrodes of conductive carbon paint (average flake size of 1 µm).*

3. Temperature dependence of Infrared and Raman spectra in the spectral region of molecular phonons

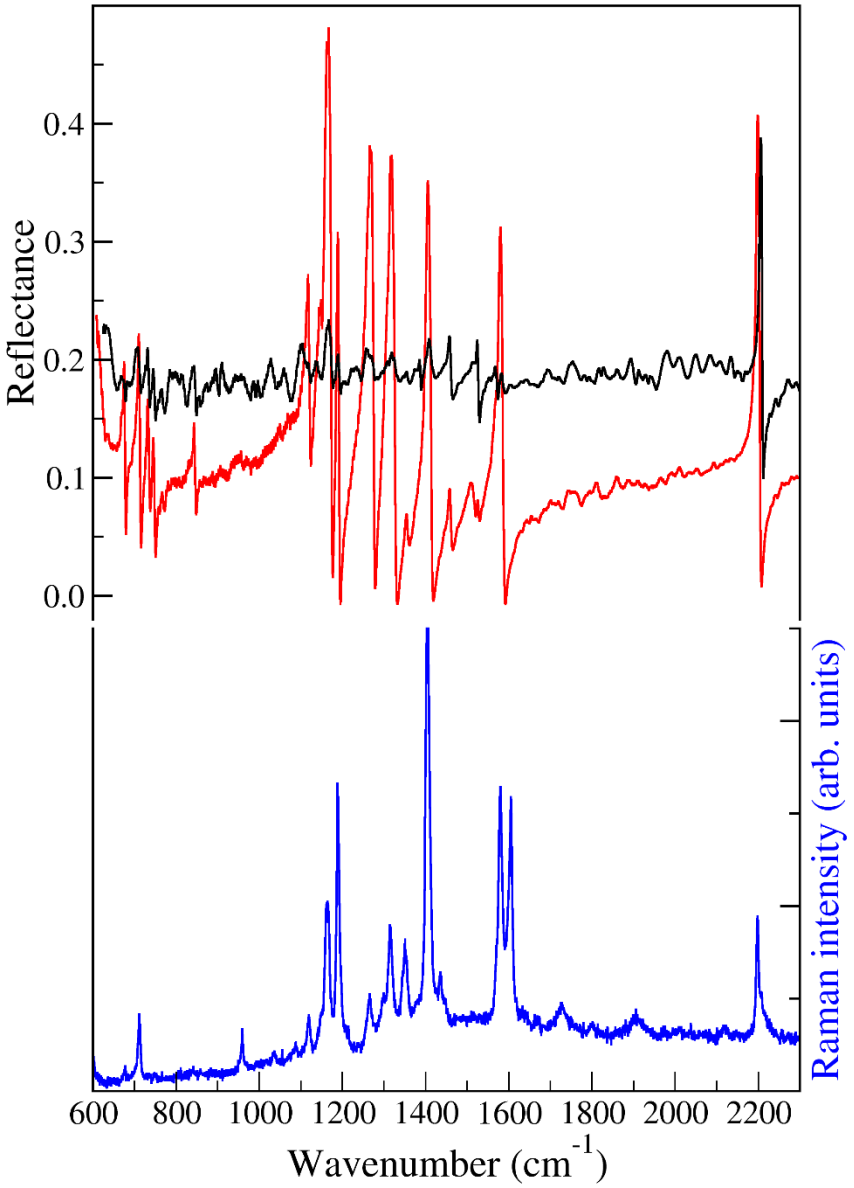

Figure S4. *Room temperature polarized IR and Raman spectra of M_2P-TCNQ. Red line: reflectance spectrum, electric vector E parallel to the c stack axis. Black line: IR spectrum, E perpendicular to c. The spectrum is offset for clarity. Blue line: Raman spectrum, (perp,perp) polarization, 647 nm exciting line. The frequency coincidence between Raman and IR bands polarized along the stack is consistent with the lack of inversion center along the stack. The charge sensitive mode $b_{1u}\nu_{20}$ of TCNQ (C=C stretching) seen in the perpendicular IR spectrum indicates an ionicity of about 0.5.*

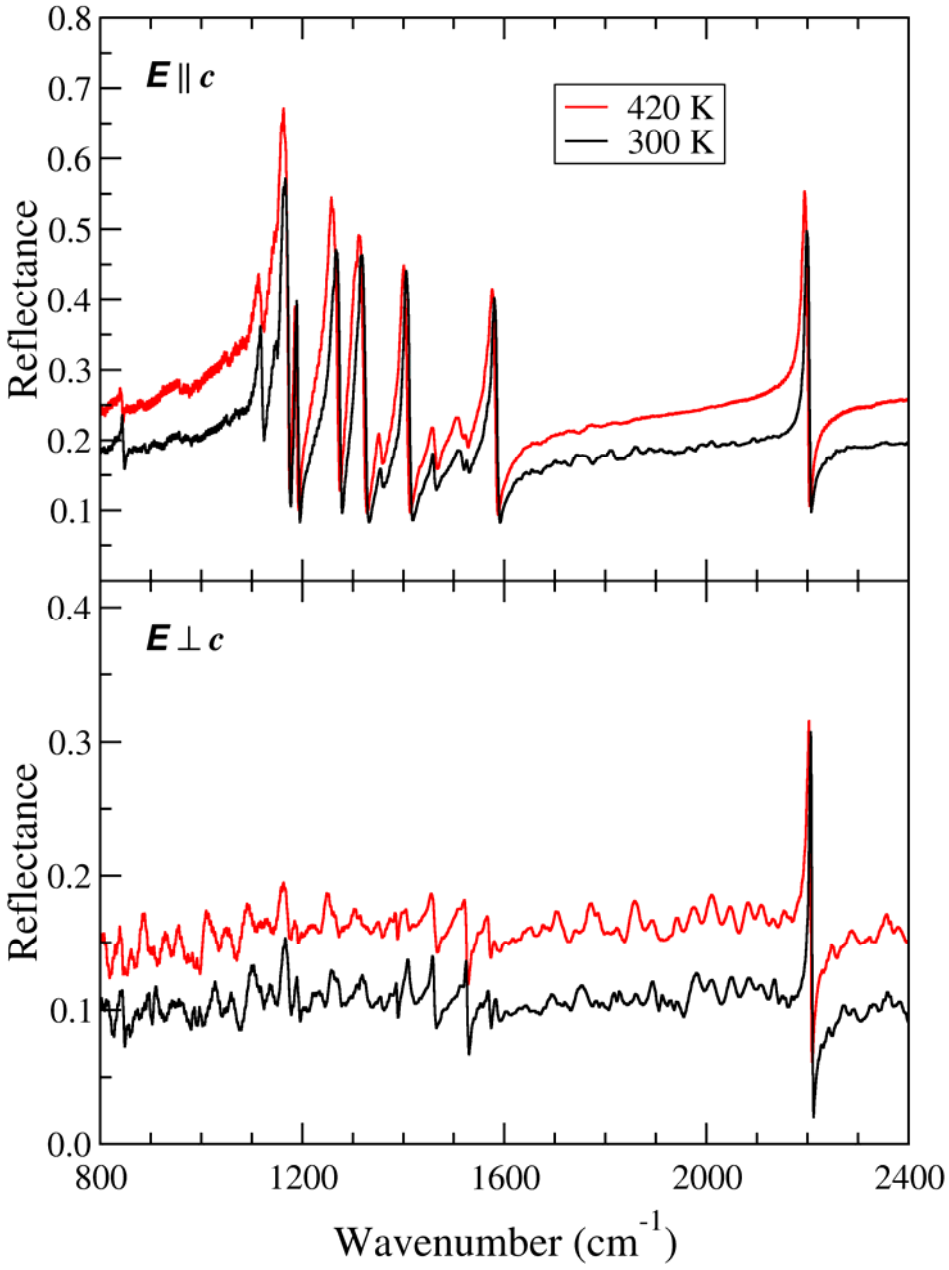

Figure S5. *Polarized IR reflectance spectra of M_2P-TCNQ at RT (black line) and 420 K (red line). The IR electric vector is parallel to the c stack axis (top) and perpendicular to it (bottom).*

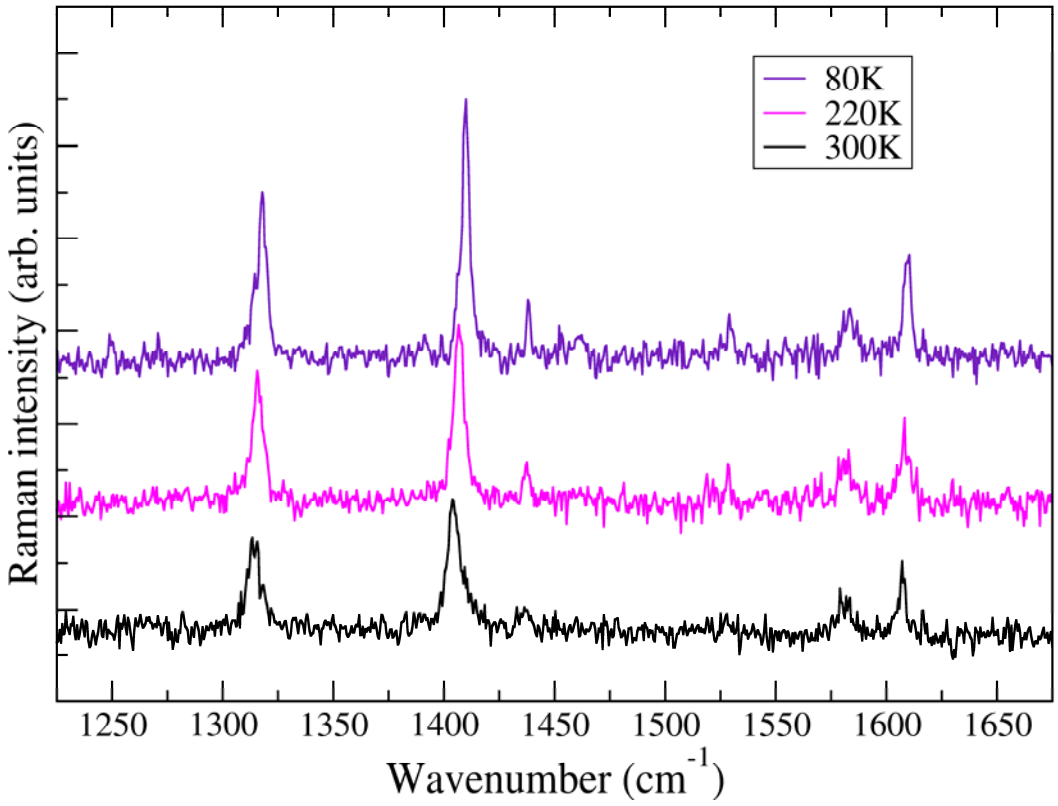

Figure S6. *Raman spectra of M_2P-TCNQ, (c,c) polarization, at RT (black line) and below. Exciting line: 752 nm.*

4. Deconvolution of the low-frequency Raman spectra as a function of temperature

The spectra (20-420 cm^{-1}) have been fitted with nine Voigt functions, starting from the 80 K spectrum in (*c,c*) polarization and going gradually up using the previous fit as a starting point. Beyond 360 K the fitting was not stable anymore. We used the open source program FITYK [M. Wojdyr, *J. Appl. Cryst.* **43**, 1126-1128 (2010)].

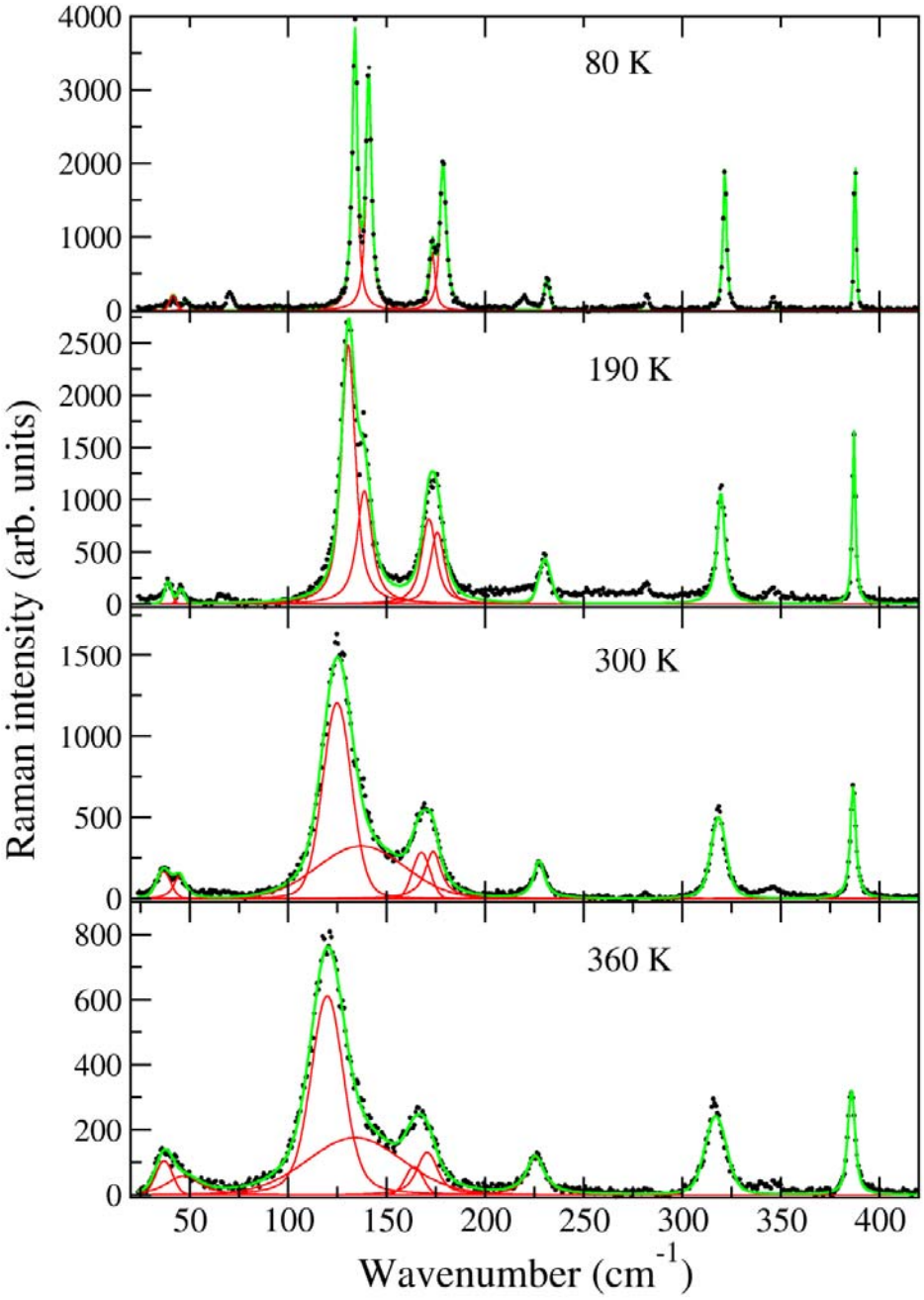

Figure S7. *Examples of curve fitting of M_2P-TCNQ low-frequency Raman spectra in (c,c) polarization, 752 nm exciting line, at four different temperatures. Dots: original spectrum; red lines: fitting functions; green line: resulting fitted spectrum.*

5. First principles calculations

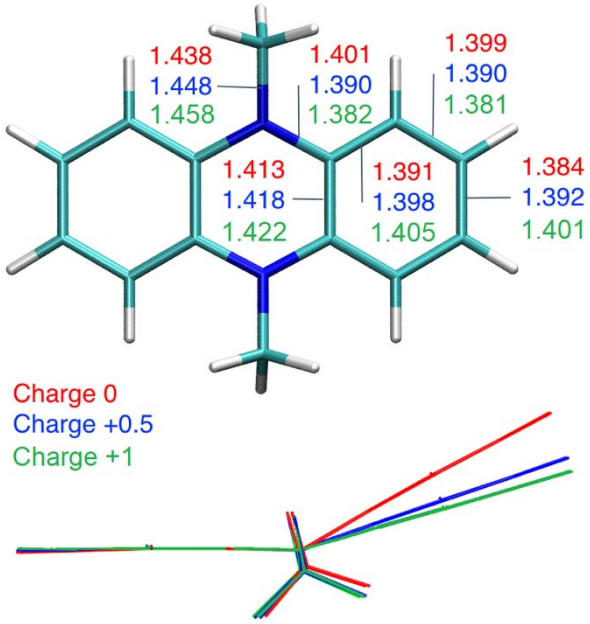

Figure S8. *Comparison of the equilibrium geometries of an isolated (gas-phase) M_2P molecule (red), cation (green) and for a fractional charge +0.5 (blue), similar to M_2P in the M_2P-TCNQ crystal. The molecular charge has a modest impact on the bond lengths, but it greatly affects the molecular shape, with M_2P becoming more planar upon charging. The "folding-angle" measures 148, 159, 163 degrees for 0, +0.5, +1 charge, respectively. DFT geometry optimizations were performed at the PBE0/6-31G* level. The geometry for +0.5 fractional charge was obtained by considering a symmetric M_2P^+ dimer cation, in which the intermolecular distance was constrained to a large value (5 nm) as to ensure negligible intermolecular interactions.*

The M_2P-TCNQ polarization has been calculated following the Berry phase approach used for the prototypical TTF-CA. We first reproduced the literature data (Giovannetti et al., PRL 103, 266401, 2009; Ishibashi et al., Physica B 405, S338, 2010), including the so-called $P(\lambda)$ curve, i.e., the plot of the polarization along the path connecting the polar (λ=1) and centrosymmetric (λ=1) structure. We applied the same procedure to M_2P-TCNQ, and Figure S9 below indeed shows that the $P(\lambda)$ curve presents a smooth behavior that ensures the absence of artifacts associated with the Berry phase calculation. Whereas $P(\lambda)$ along the stack is in-line with the TTF-CA result, we obtain comparable values of P also along the a axis, perpendicular to the stack. This unexpected result (if compared to the axial polarization in TTF-CA) has been subject of accurate checking.

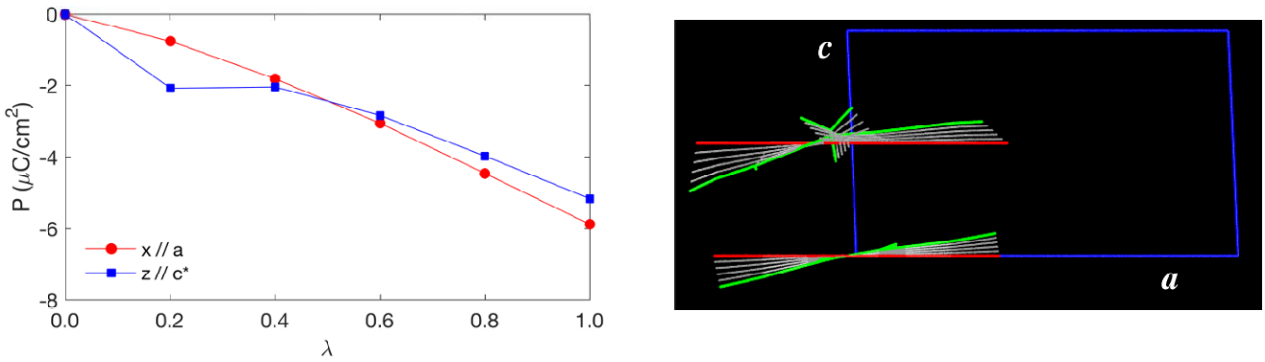

Figure S9. *Left: Polarization of the M_2P-TCNQ crystal calculated along the path connecting the experimental polar structure (λ=1) and the reference centrosymmetric structure (λ=0). Calculation performed at the PBE0/6-311G* level with the CRYSTAL17 code. Right: Visualization of the structures employed in the calculations of the spontaneous polarization, i.e., the polar structure (green), the centrosymmetric structure (red) and the intermediate ones (gray). Only the asymmetric unit is shown.*

We first remark that the polarization quantum amounts to 17.3 and 10.6 μC/cm^2 along *a* and *c**, respectively, so that jumps to another branch of the polarization lattice would be easily detectable on Fig. S9's scale. Moreover, consistent *P*(λ) curves have been confirmed with different Brillouin-zone sampling zone (4x4x4, 6x6x6, 8x8x8), lifting any reasonable doubt on the validity of our calculation. We have then tested several hypotheses for the origin of the unexpected polarization along *a* with explicit calculations. This includes finite-system calculations (e.g. considering molecular TCNQ-M_2P-TCNQ trimers extracted from the crystal structure) and solid-state periodic calculations. The latter include Berry phase calculations as a function of motivated structural deformations, including the relative shift along *a* of the D and A sublattices, the rigid rotation of M_2P along the NN axis, and the rotation of the M_2P methyl groups. The first two deformations were supposed to affect intermolecular CT network, the latter was intended to perturb the weak hydrogens bonds formed by methyl H. None of these attempts provided useful insight for the rationalization of the large *a*-axis component of the polarization.